

Nanoscale

rsc.li/nanoscale



ISSN 2040-3372



ROYAL SOCIETY
OF CHEMISTRY

Celebrating
IYPT 2019

PAPER

Hyuck Choo *et al.*

Enhanced broadband fluorescence detection of nucleic acids using multipolar gap-plasmons on biomimetic Au metasurfaces



NCNST

Cite this: *Nanoscale*, 2019, **11**, 13750

Enhanced broadband fluorescence detection of nucleic acids using multipolar gap-plasmons on biomimetic Au metasurfaces†

 Vinayak Narasimhan,^a Radwanul Hasan Siddique,^a Magnus Hoffmann,^b
 Shailabh Kumar^a and Hyuck Choo^{*,a}

Recent studies on metal–insulator–metal-based plasmonic antennas have shown that emitters could couple with higher-order gap-plasmon modes in sub-10-nm gaps to overcome quenching. However, these gaps are often physically inaccessible for functionalization and are not scalably manufacturable. Here, using a simple biomimetic batch-fabrication, a plasmonic metasurface is created consisting of closely-coupled nanodisks and nanoholes in a metal–insulator–metal arrangement. The quadrupolar mode of this system exhibits strong broadband resonance in the visible-near-infrared regime with minimal absorptive losses and effectively suppresses quenching, making it highly suitable for broadband plasmon-enhanced fluorescence. Functionalizing the accessible insulator nanogap, analytes are selectively immobilized onto the plasmonic hotspot enabling highly-localized detection. Sensing the streptavidin–biotin complex, a 91-, 288-, 403- and 501-fold fluorescence enhancement is observed for Alexa Fluor 555, 647, 750 and 790, respectively. Finally, the detection of single-stranded DNA (*gag*, *CD4* and *CCR5*) analogues of genes studied in the pathogenesis of HIV-1 between 10 pM–10 μM concentrations and then *CD4* mRNA in the lysate of transiently-transfected cells with a 5.4-fold increase in fluorescence intensity relative to an untransfected control is demonstrated. This outcome promises the use of biomimetic Au metasurfaces as platforms for robust detection of low-abundance nucleic acids.

 Received 13th April 2019,
 Accepted 18th May 2019
 DOI: 10.1039/c9nr03178b
 rsc.li/nanoscale

Introduction

Optical field-enhancing plasmonic environments that influence the decay lifetimes of quantum emitters were first proposed theoretically by Purcell¹ and demonstrated experimentally in various efforts.^{2,3} Through sub-wavelength light confinement, plasmonic nanostructures greatly increase the intensity of localized electromagnetic fields, thereby enhancing excitation characteristics of emitters proximal to them.⁴ However, emitters within 10 nm from the nanostructures couple to non-radiative, dark higher-order plasmonic modes, and the energy is dissipated through non-radiative channels that lead to rapid quenching of the far-field emission.^{5,6} Recent research of plasmonic nanogaps has revealed that emitters can effectively couple with hybridized higher-order gap-plasmon modes to overcome quenching effects.^{7–9} Modes that are otherwise dark in isolated nanostructures such as nano-

particles become highly radiative in plasmonic nanogaps.⁹ Furthermore, increased electric field lifetimes and reduced radiative losses supported by higher-order plasmonic modes can greatly benefit applications such as plasmon-enhanced fluorescence.¹⁰ However, while recent literature has demonstrated nano-architectures capable of overcoming quenching, their use in applications such as multiplexed biosensing remains largely unexplored. This could be attributed to diminutive surface areas of the hotspots or physical inaccessibility of nanogaps for functionalization as well as challenges involved in reliably reproducing nanoscale gaps, especially in large scale, batch fabrication.¹¹

In this work, using a simple three-step biomimetic fabrication process, we have created a highly scalable plasmonic metasurface (MS) consisting of a short-range ordered array of closely coupled gold (Au) nanodisks on nanoholes separated by a 5 nm silica (SiO₂) nanogap with a large accessible hotspot surface area for biosensing (Fig. 1). This metal–insulator–metal metasurface (MIM-MS) configuration whose geometry can be tuned by adjusting process parameters was found to efficiently scatter from the visible to the near-infrared (VIS-NIR) range. Furthermore, the SiO₂ nanogap can be selectively functionalized to bind molecules of interest presenting an advantage over conventional Au nanostructures.¹² Our in-

^aDepartment of Medical Engineering, California Institute of Technology, Pasadena, CA 91125, USA. E-mail: hchoo@caltech.edu, hyuck.choo@samsung.com

^bDepartment of Biology and Biological Engineering, California Institute of Technology, Pasadena, CA 91125, USA

†Electronic supplementary information (ESI) available. See DOI: 10.1039/c9nr03178b

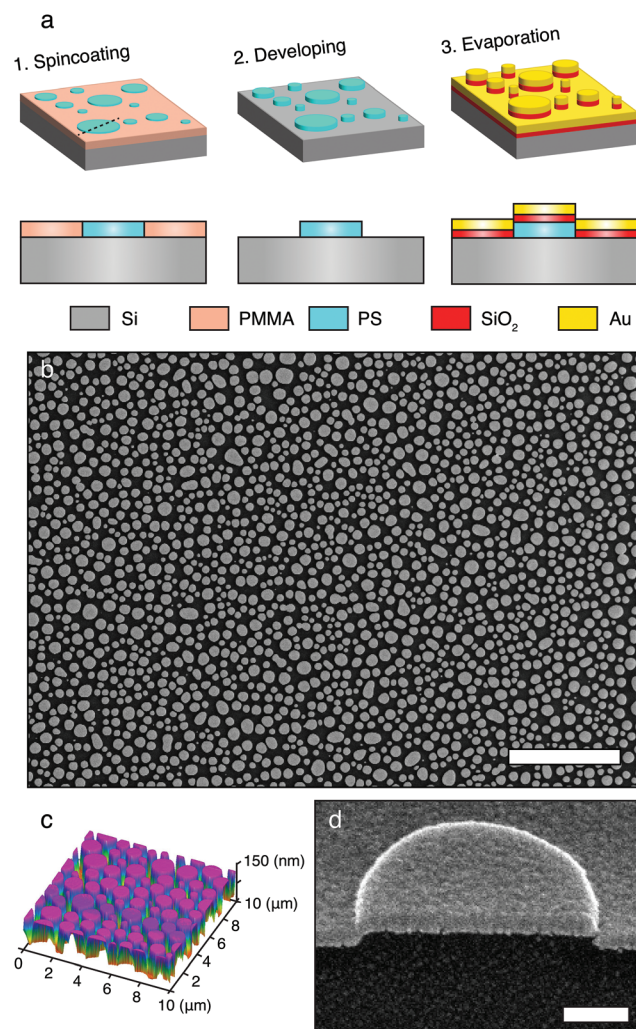


Fig. 1 (a) Fabrication of the MIM-MS through a simple three-step biomimetic phase separation fabrication process. Cross-sectional view is shown as indicated by the dotted line. (b) Top view SEM image of the metasurface showing circular/ellipsoidal MIM pillars. Scale: 10 μm . (c) 3D AFM image of a 10 \times 10 μm area of the MIM-MS which shows a high degree of height uniformity. (d) A cross-sectional SEM image of an individual MIM scatterer with a clearly visible 5 nm nanogap. Scale: 200 nm.

depth study of an individual MIM scatterer reveals that the higher-order quadrupolar mode ($l = 2$) of this architecture is radiant, and emitters can effectively couple into this mode, resulting in enhanced quantum emissions (Fig. S1†). Furthermore, we have experimentally verified the suppression of quenching and broadband fluorescence enhancement of the $l = 2$ mode resonance in the VIS-NIR regime for quantum emitters within 10 nm from the nanogap, and consequently, the broad resonance profile of the $l = 2$ mode resonance can support plasmon-enhanced fluorescence when compared to isolated nanostructures favoring multiplexed biosensing using different fluorophores on the same platform.

In our experiments, we have utilized oligonucleotide-based biosensing that is now of great interest.^{13,14} These single-stranded DNA (ssDNA) or RNA are often less than 5 nm in size

when folded, and they can be placed within the regime of strong quenching.¹⁵ By suppressing quenching, we demonstrate robust biosensing of nucleic acid sequences of various sizes at concentrations comparable to the resolution of commercial RNA quantitation assays.¹⁶ Through fluorescent hybridization, ssDNA analogues of the human immunodeficiency virus type 1 (HIV-1) receptor genes *CD4* and *CCR5*, as well as the HIV-1 gene *gag*, were detected. Finally, the *CD4* mRNA was detected in the lysate of transiently-transfected cells demonstrating the versatility and specificity of the MIM-MS as a quantitative biosensor.

Experimental methods

Biomimetic phase-separation through polymer blends

Poly(methyl methacrylate) (PMMA, $M_w = 9590$, Polymer Standards Service GmbH, Germany) and polystyrene (PS, $M_w = 19\,100$, Polymer Standards Service GmbH, Germany) were dissolved in methyl ethyl ketone (MEK, Sigma-Aldrich, USA) with mass ratios of 75% : 25%, 65% : 35% and 55% : 45% to fabricate the three samples with mean diameters of 195 nm, 340 nm and 645 nm respectively. The solution concentrations were 20 mg mL^{-1} . Solutions were spin-coated at a spin-speed of 3500 rpm and acceleration of 2000 rpm for 30 s. Relative humidity was maintained between 40%–50% during the spin-coating. The de-mixing of the blend components occurs during spin coating due to the difference in relative solubility of PS and PMMA in MEK.^{17,18} First, water condensation begins at humidity levels above 35% forming a water-rich layer at the air/solution interface due to the difference in evaporation rate between water and MEK. Water starts to condense from the air into the solution because of the evaporation of MEK decreasing the temperature on the top below the dew point. Due to the high water concentration, a 3D phase separation occurs between PS/MEK and PMMA/MEK/water. Upon drying, a purely lateral morphology is formed with ellipsoidal PS islands in a PMMA matrix. The samples were then rinsed in acetic acid for 2 min and dried in a stream of N_2 to remove the PMMA matrix leaving behind the PS islands.

High-resolution imaging and statistical analysis of the MIM-MS

High-resolution SEM imaging was performed on the MIM-MS samples using a Nova 200 Nanolab Dualbeam microscope (FEI, USA) at 5 kV while AFM imaging was performed using a Bruker Dimension ICON AFM (Bruker, Germany) using a 100 μm long monolithic silicon cantilever (BudgetSensors) under ambient laboratory conditions using tapping mode with a resonance frequency of about 350 kHz. ImageJ (National Institutes of Health, USA), a public-domain and Java-based image processing tool was used for the statistical analysis of the MIM-MS surface. Every pixel in the acquired SEM images were converted to black or white based on a thresholding condition that was obtained by calculating the mean intensity value of all pixels of the image. Following this, the diameter distribution of the MIM scatterers was determined.

Optical simulations of the MIM-MS

Optical simulations of a single MIM scatterer as well as the MIM-MS as a whole were performed using a 3D finite-difference time-domain software (Lumerical Solutions, Canada). A combination of periodic and perfect matching layer (PML) boundary conditions along with a total-field scattered-field (TFSF) source was used. The absorption cross section was obtained in the total field region inside the TFSF source while the scattering cross section was obtained in the scattered field region outside the TFSF source. For the quantum yield simulations, a dipole source was placed at various distances from the plasmonic hotspot. The radiative and total decay rates were measured as a function of the amount of radiation leaving the system and the total power injected by the dipole source respectively. These measurements were made by means of a transmission box placed around the structure and the dipole source. The quantum yield q of the emitter in the presence of the MIM scatterer was then computed as $q = \gamma_r / (\gamma_r + \gamma_{nr} + \gamma_{abs})$ where γ_r and γ_{nr} are the radiative and non-radiative decay rates while γ_{abs} corresponds to absorptive losses. Finally, the enhancement factor was computed as $EF = q/q_o \times |E|^2/|E_o|^2$ where q_o is the intrinsic quantum yield of the fluorophore and $|E|^2/|E_o|^2$ is the normalized electric-field enhancement at the location of the emitter due to the MIM scatterer.

Optical spectroscopic analysis of the MIM-MS

A customized optical microscope operating in dark-field (DF) mode was used for the micro-spectroscopic investigation of the fabricated MIM-MS samples. A halogen lamp was used as a light source using a 100 \times objective with a numerical aperture of NA = 0.90. The scattered light was collected in a confocal configuration and analyzed using a spectrometer (AvaSpec-ULS2048x64-USB2). A 400 μ m core optical fiber was used to obtain a spatial resolution of 20 μ m to characterize the scattering of the MIM-MS.

Streptavidin–biotin complex assay preparation

Lyophilized SH-PEG-biotin of varying PEG lengths (Nanocs, Inc., USA) were dissolved in 90% ethanol at concentrations greater than 10 mg mL⁻¹. Then, the solution was added to the MIM-MS and glass slide control surfaces for a 2 h incubation at room temperature (RT). The samples were then washed in deionized (DI) water for 30 min. Streptavidin conjugates (ThermoFisher Scientific, USA) at a working concentration of 0.5 mg mL⁻¹ in phosphate-buffered saline (PBS) were added to the MIM-MS surface for a 1 h incubation at RT. Following this, the samples were washed again in DI water for 30 min and prepared for imaging.

NHS ester assay preparation

First, the MIM-MS and glass slide control samples were incubated for 1 h in 4% APTES (Sigma-Aldrich, USA) dissolved in acetone. After washing in acetone, the NHS ester of AF647 (ThermoFisher Scientific, USA) at a concentration of 2 mg mL⁻¹ in dimethyl sulfoxide (Sigma-Aldrich, USA) was added to

the substrate for 3 h. Following this, the samples were washed in DI water for 30 min and prepared for imaging.

SsDNA and mRNA hybridization

The capture oligo was bound to the MIM-MS through the crosslinking of two primary –NH₂ groups. The capture oligo was designed with an –NH₂ group at the 3'-end. The SiO₂ insulator layer of the MIM-MS was functionalized with APTES. The two primary –NH₂ groups on the APTES functionalization and the capture oligo are linked by means of a water soluble cross-linker (bis(sulfosuccinimidyl)suberate) (BS3). Once the capture oligo was bound to the SiO₂ layer, the ssDNA/mRNA target molecules diluted to the working concentration in a hybridization buffer (Molecular Technologies, USA) were dispensed on the substrate. First, the MIM-MS samples were incubated for 1 h in 4% APTES (Sigma-Aldrich, USA) dissolved in acetone. After washing in acetone, BS3 (Sigma-Aldrich, USA) dissolved at a 50 \times molar excess to the capture oligo concentration in a coupling buffer (100 mM sodium phosphate, 0.15 M sodium chloride, pH 7.2) was added to the MIM-MS samples for 15 min. Next, the capture oligo (Integrated DNA Technologies, Inc., USA) diluted to a working concentration of 20 μ M in a folding buffer (137 mM sodium chloride, 2.7 mM potassium chloride, 8 mM sodium phosphate dibasic, 2 mM potassium phosphate monobasic, pH 7.5) was added to the MIM-MS samples for 1 h. After washing in folding buffer, the target sequence (100 bp sequence purchased from Integrated DNA Technologies/full-length CD4 ssDNA synthesized through PCR/CD4 mRNA from total RNA in lysate) in a probe hybridization buffer (Molecular Technologies, USA) was added to the MIM-MS. Hybridization buffer with 10% formamide was used for the 100 bp and full-length sequence while 15% formamide was used for the mRNA. The samples were incubated overnight (O/N) at 37 °C and 45 °C for the 100 bp/full-length sequence and the mRNA respectively. Following washing with a probe wash buffer (Molecular Technologies, USA), the detection oligo (Integrated DNA Technologies, Inc., USA) diluted to a working concentration of 10 μ M in hybridization buffer with 10% or 15% formamide depending upon the target sequence was added to the MIM-MS. The samples were then incubated O/N at 37 °C or 45 °C. Finally, excess detection probes were removed with wash buffer.

CD4 ssDNA synthesis

Full-length CD4 ssDNA was generated by a two-step PCR protocol. For the first reaction, full-length CD4 double-stranded cDNA (Accession NM_000616.4, NCBI) was amplified from the lentiviral plasmid Phage2-CMV-CD4 using CD4 Fwd 5'-ATGAACCGGGGAGTCCCTTTTAG-3' and CD4 Rev 5'-TCAAATGGGGCTACATGCTTCTG-3' primers. The CD4 cDNA product was purified by DNA agarose gel electrophoresis and was used as template for the second PCR reaction to generate CD4 ssDNA. For this reaction, only the CD4 Fwd primer was used to generate ssDNA copies of the coding strand of CD4. The final product was purified using a PCR purification kit (Qiagen, Germany) and subsequently concentrated using NanoSep cen-

trifugal devices (Pall, USA). For chimeric *CCR5-CD4* ssDNA molecules, nucleotides 1–56 of *CD4* were replaced with nucleotides 1–56 of *CCR5*. *CCR5-CD4* ssDNA was generated with the above protocol using the *CCR5-CD4* Fwd primer 5'-ATGGATTATCAAGTGTCAAGTCCAATCTATGACATCAATTATTATACATCGGAGCCCCCAGCAGCCACTCAGG-3' for the second PCR reaction.

Total RNA extraction from Expi293 cells

Expi293 cells (ThermoFisher Scientific, USA) were transiently-transfected with the Phage2-CMV-CD4 plasmid using the transfection reagent ExpiFectamine (ThermoFisher Scientific, USA) in accordance with the manufacturer's guidelines. The cells were incubated at 37 °C and 5% CO₂ under shaking conditions at 470 rpm. Control and transfected cells were harvested after 48 h incubation and centrifuged at 400g for 10 min. The supernatants were removed and the pellets were re-suspended in 10 mL TRIzol (ThermoFisher Scientific, USA) to lyse the cells. Total RNA was isolated from the cell lysate using Direct-zol RNA extraction kits (Zymo Research, USA) and concentrated using NanoSep centrifugal devices (Pall, USA).

CD4 quantification by flow cytometry

CD4 expression on transiently-transfected Expi293 cells was detected by flow cytometry (MACSQuant Analyzer 10, Miltenyi Biotec, Germany). Cells were stained using an APC-conjugated anti-CD4 antibody (Cat. no. MHC0405, ThermoFisher Scientific, USA, 1:100 dilution) in PBS containing 2% fetal bovine serum (FBS) for 30 min at RT and washed twice before analysis.

Fluorescence microscopy and image processing

All fluorescence imaging was conducted on using a Leica DMI 600 wide field microscope (Leica Camera AG, Germany) with a 100× objective (NA = 1.40, immersion medium = oil). For imaging AF555 and AF647, a Lumencor SPECTRA X (Lumencor, Inc., USA) illumination system was used while for AF750 and AF790, a separate LED for Cy7 excitation (ThorLabs, USA) was used. ImageJ was used to obtain the fluorescence enhancement factors. Selecting individual MIM scatterers from each image, the mean fluorescence intensity from a region of interest (ROI) spanning the 2D area of the ring-shaped hotspot was computed. Using the same ROI area, the mean fluorescence from corresponding glass slide controls were obtained. Background signal was obtained using respective substrates with no added fluorophores and was subtracted from the images during fluorescence intensity analysis.

Results and discussion

The MIM-MS was fabricated using a simple three-step process, as illustrated in Fig. 1a. The first step involves a biomimetic phase-separation technique analogous to the processes that form biophotonic nanostructures on the wings and scales of birds and insects.¹⁹ It has been posited that in nature, these nanostructures are self-assembled through a phase separation

of biopolymers in the amphiphilic phospholipid bilayer of scale cells, followed by chitin deposition in the extracellular space.¹⁹ Here, we rely on the phase separation of a synthetic polymer blend of polystyrene (PS) and polymethyl methacrylate (PMMA) co-dissolved in methyl ethyl ketone (MEK) under spin-coating.^{17,18,20} Due to differences in polarity and solubility of PS and PMMA along with varying evaporation rates of MEK and water, under specific humidity conditions, the PS/PMMA/MEK system undergoes a lateral phase separation which results in densely packed circular islands of PS in a matrix of PMMA (Fig. S2†). Next, through selective dissolution of PMMA in acetic acid, we create isolated pillars of PS. Finally, we directionally evaporated SiO₂ and Au to form the plasmonic MIM-MS as shown in the scanning electron microscopy (SEM) image in Fig. 1b. The atomic force microscopy (AFM) profiling of the surface reveals a highly uniform structural height (Fig. 1c). Furthermore, we were able to achieve MIM nanogaps of 5 nm through this simple and highly scalable process (Fig. 1d).

To better elucidate the resonance profile of the MIM-MS, we simulated the scattering response of a single MIM structure. A schematic of the structure is shown in Fig. 2a. As explained by mode hybridization theory, strong coupling between the two metal layers (in this case a disk and hole) with a sandwiched insulator in-between them results in strong field confinement that leads to strong scattering in the far-field (Fig. 2a).²¹ First, to determine the gap-plasmon modes of the single MIM structure, we performed three-dimensional (3D) finite-difference-time-domain (FDTD) simulations to obtain the scattering cross section in the VIS-NIR regime between 500–2500 nm. By varying the diameter of structure, we observe the origination of the first-order ($l = 1$) and subsequently, the second-order ($l = 2$) gap-mode as seen in Fig. 2b. The $l = 1$ mode for larger structures (diameter: 200–500 nm) is in the mid-IR and is therefore inaccessible for most fluorescence-based applications. However, being in the VIS-NIR regime, the $l = 2$ mode could potentially be utilized for fluorescence enhancement. Further analysis of the structure's scattering profile in the VIS-NIR regime between 300–800 nm is shown in Fig. 2c. The field profiles of the three gap-modes as shown in Fig. 2d indicate that $l = 1, 2$, and 3 corresponding to longitudinal dipolar, quadrupolar, and hexapolar anti-bonding bright modes, respectively.

The resonance profile of the $l = 2$ mode is broader for larger MIM structures compared to the $l = 1$ mode for smaller structures. The full width at half maximum (FWHM) of the $l = 2$ mode for the 300 nm (FWHM ~ 96 nm), 400 nm (FWHM ~ 157 nm), and 500 nm (FWHM ~ 197 nm) structures were 1.5, 2.4, and 3 times, respectively, that of the $l = 1$ mode for the 100 nm structure (FWHM ~ 66 nm). Additionally, smaller structures display considerably more absorption than scattering (Fig. S1†).^{22,23} However, a large scattering cross-section is desirable for applications based on light-scattering microscopy such as plasmon-enhanced fluorescence-based biosensing.²⁴ Fig. 2e compares the ratio of the scattering and absorption components of the extinction ($C_{\text{scat}}/C_{\text{abs}}$) for the $l = 1$ mode of

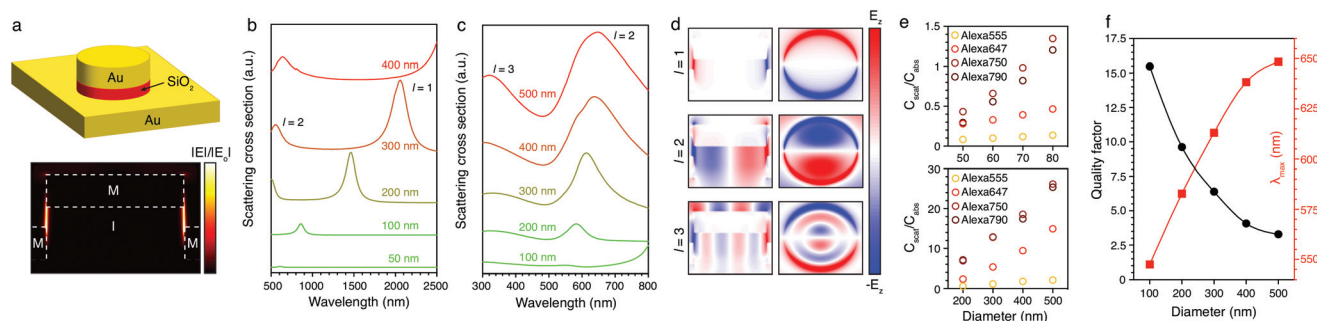


Fig. 2 (a) A schematic of the MIM configuration consisting of an Au nanodisk closely coupled with an Au nanohole separated by an SiO₂ nanogap. (b) Scattering cross section of a single MIM scatterer for different diameters from 50 nm to 400 nm. The first-order ($l = 1$) and second-order ($l = 2$) gap modes are both radiant. (c) Scattering cross sections of the second-order ($l = 2$) and third-order ($l = 3$) modes of single MIM scatterers in the VIS-NIR regime. (d) The field profile of the nanogap shows the presence of a dipolar ($l = 1$), quadrupolar ($l = 2$) and hexapolar ($l = 3$) anti-bonding bright gap modes. (e) The ratio of the scattering and absorption components of the extinction $C_{\text{scat}}/C_{\text{abs}}$ for the $l = 1$ mode of small MIM scatterers (top) compared with that of the $l = 2$ mode of larger MIM scatterers (bottom). (f) The quality factor (black) and plasmon resonance wavelength (red) for the $l = 2$ mode of larger MIM scatterers.

smaller MIM structures with the $l = 2$ mode of larger MIM structures for fluorophores used in this work. The $C_{\text{scat}}/C_{\text{abs}}$ ratio is an order of magnitude larger in the case of the latter. However, as shown in Fig. 2f, increasing the MIM structure diameter also lowers the quality factor of the plasmon resonance. Therefore, using a geometry that is between 200–400 nm in diameter would be optimal for plasmon-enhanced fluorescence as it supports broadband resonance with a high $C_{\text{scat}}/C_{\text{abs}}$ ratio without sacrificing on the quality factor.

By varying the relative mass ratios of the PS and PMMA, we realized MIM-MS of structurally-induced varying coloration with a high chromaticity. Green, orange, and red surfaces were generated (Fig. 3a) by controlling the average size of the MIM scatterers in the distribution with mean diameters being 195 nm, 340 nm, and 645 nm, respectively (Fig. 3b). Using an optical

micro-spectroscopic setup in dark-field (DF) mode, the scattering spectral response of each of the three plasmonic metasurfaces was obtained. Matching their macroscopic appearance, the metasurfaces displayed scattering resonances with maximas at 555 nm, 636 nm, and 792 nm as shown in Fig. 3c.

3D FDTD simulations were performed on a 4 μm by 4 μm spatial array of MIM scatterers matching the size and spatial periodicity of the fabricated samples (Fig. 3d). The FDTD simulation results confirm similar resonance profiles as the DF measurements indicating the presence of highly-radiant higher-order modes that scatter strongly to the far-field (Fig. 3e).

Leveraging the tunable quadrupolar resonant mode of the MIM-MS, we experimentally demonstrate broadband multiplexed fluorescence enhancement by sensing the streptavidin-biotin complex. We chose the geometry with a mean diameter of 340 nm (orange sample as shown in Fig. 3) due to its broadband scattering response centered at 636 nm, making it ideal for the 550–850 nm wavelength range. The MIM-MS were designed with SiO₂ as the insulator layer as it can be easily functionalized with a silane (–SH) group to bind with analytes of interest at the plasmonic hotspot.

The streptavidin-biotin complex plays a crucial role in numerous laboratory methods for the detection of low-concentration proteins and nucleic acids.²⁵ For instance, streptavidin conjugates bind strongly to biotinylated probes such as secondary antibodies to improve the signals from molecules expressed in low concentrations in whole samples.²⁶ By further enhancing the signal from the conjugated reporters through broadband plasmon-enhanced fluorescence, the detection limit of analytes at low concentrations can be greatly improved.

First, we functionalized the metasurface with silane-polyethylene glycol-biotin (SH-PEG-biotin) and detected different fluorescent conjugates of the protein streptavidin. The fluorescent conjugates used were Alexa Fluor 555 (AF555, excitation (ex)/emission (em) – 555/580 nm), Alexa Fluor 647 (AF647, ex/em – 650/665 nm), Alexa Fluor 750 (AF750, ex/em – 749/775 nm) and Alexa Fluor 790 (AF790, ex/em – 784/814 nm). The

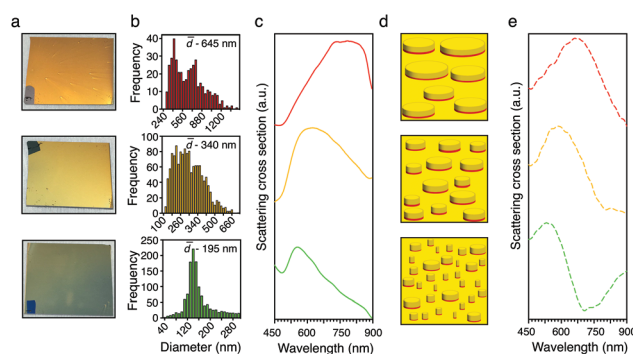


Fig. 3 (a) Stable and tunable structurally-induced coloration with high chromaticity is obtained using the biomimetic fabrication technique. (b) MIM-MS with a mean diameter of 195 nm, 340 nm, and 645 nm resulted in green, yellow and red structural colors, respectively. (c) The far-field scattering profile of the three MIM-MS measured through DF microscopy shows resonance profiles with maximas at 555 nm, 636 nm, and 792 nm, respectively. (d), (e) 3D FDTD simulations of a 4 μm \times 4 μm array of the MIM-MS matching the geometry of the three fabricated samples shows a good correlation with the experimentally measured scattering results.

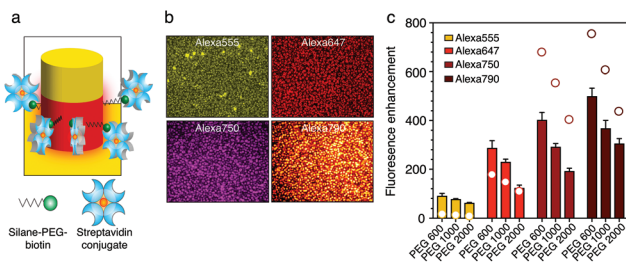


Fig. 4 (a) A schematic of the selective streptavidin–biotin detection. (b) Multiplexed biosensing of streptavidin conjugated with AF555, AF647, AF750, and AF790 fluorophores. (c) Broadband fluorescence enhancement relative to a glass control for different streptavidin conjugates with varying PEG lengths. The numerical enhancement factor for each case computed through FDTD is plotted as dots.

schematic of the experiment is shown in Fig. 4a. The plasmon-enhanced fluorescence from a multiplexed assay consisting of all the aforementioned streptavidin conjugates is shown in Fig. 4b. The ring-shaped distribution corresponding to plasmonic hotspots of individual MIM scatterers is clearly visible.

Next, by varying the PEG molecular weight from 600 Da–2000 Da, we adjusted the chain length and consequently the distance of the fluorophores from the hotspot between 7–11 nm.²⁷ The distance was estimated by summing the chain length of the PEG and the size of a streptavidin tetramer.²⁸ We then measured the fluorescence intensity for each sample and normalized it relative to a control glass sample prepared under the same conditions. As the PEG length was shortened, the observed fluorescence enhancement for each fluorophore relative to the corresponding control increased (Fig. 4c). In all cases, a fixed concentration of the silane-PEG-biotin and streptavidin were used. For PEG 600, enhancement factors of 91-, 288-, 403-, and 501-fold were observed for AF555, AF647, AF750, and AF790, respectively. To further test the suppression of quenching we directly bound AF647 to the SiO₂ layer (*i.e.* emitter distance \sim 0 nm). This was achieved through silanization of the SiO₂ layer with (3-aminopropyl)triethoxysilane (APTES) and subsequent labeling of the free primary amine ($-NH_2$) end with the *N*-hydroxysuccinimide (NHS) ester of AF647. An enhancement factor of 586-fold was obtained in this case, indicating strong suppression of quenching. All the experimental results were in good agreement with enhancement factors that were numerically computed using FDTD (Fig. 4c and Fig. S3†). We also modeled the radiative and non-radiative decay rates associated with quantum emitters placed at various distances from a single MIM scatterer (Fig. S4†) and compared them with those of an isolated nanostructure (Fig. S5†). The first-order dipolar mode of the isolated nanostructure quenches the emitter as it moves closer to the structure while the MIM scatterer effectively suppresses quenching.

To demonstrate the utility of the MIM-MS as a biosensor, we targeted the detection of the HIV-1 *gag*, *CD4*, and *CCR5* genes popularly studied in the pathogenesis of HIV-1. They encode the Gag, CD4, and CCR5 proteins respectively. Gag is a structural polyprotein that is essential for virion assembly as it

forms the capsid that encapsulates the viral genome HIV-1.²⁹ Gag is routinely used as a marker for the detection of HIV-1-infected cells³⁰ and the quantification of HIV-1 virion production.³¹ CD4 is primarily expressed on CD4+ T-lymphocytes and functions as co-receptor to the T-cell receptor during antigen presentation.³² CCR5 is a G-protein-coupled receptor (GPCR) found on the surface of various immune cells, including T lymphocytes, macrophages and dendritic cells.³² HIV-1 predominantly infects CD4+ T-lymphocytes through interactions with CD4 and a co-receptor, which during early infection is almost exclusively CCR5.³³ Therefore, a threshold level of CD4 and CCR5 receptors is required to support the infection.^{34,35} While CD4 is abundantly expressed on CD4+ T-cells, its expression fluctuates on macrophages³⁶ and CD34+ hematopoietic stem cells,³⁷ making them also potentially susceptible to HIV-1 infection. Moreover, CCR5 expression is highly variable on different subsets of immune cells and depends on the cell maturation state.³⁴ Consequently, studying the expression of HIV-1 *gag*, *CD4*, and *CCR5* in parallel through selective capture and quantification could provide important information about the interplay of HIV-1 receptor expression levels and susceptibility to infection.

To selectively immobilize and detect the *gag*, *CD4* and *CCR5* nucleic acids on the MIM-MS, we utilized DNA/RNA hybridization reactions in a sandwich assay format. The target nucleic acid would first be immobilized on the plasmonic hotspot by means of a capture oligonucleotide and then detected with a fluorescently-labeled detection oligonucleotide (Fig. 5a). To test the sandwich assay, we selected the first 100 base pairs (bp) of the coding strand in the target complementary DNA (cDNA) sequences. Then, using a nucleic acid analysis software (NUPACK) to avoid secondary structure formations, we selected the binding sites for the complementary capture and detection oligos (Fig. S6†).³⁸ Following hybridization, the detection oligo conjugated with AF555 (*gag*), AF647 (*CD4*), and AF750 (*CCR5*) at the 5'-end is bound to the target sequence. Fig. 5b shows multiplexed detection of *gag*, *CD4*, and *CCR5* 100 bp ssDNA sequences at a concentration of 100 nM.

For the remainder of the study, the *CD4* gene was chosen as a representative to study the MIM-MS biosensing specificity in more detail. Fig. 5c and Fig. S7† show capture and detection of the *CD4* 100 bp ssDNA from a concentration of 10 pM to 10 μ M. Overcoming quenching, we also demonstrate the sensing of just the detection oligo (20 bp) at concentrations as low as 10 pM (Fig. S8†). Next, an ssDNA analogue of the full-length *CD4* cDNA coding strand (1377 bp) was generated through a two-step PCR protocol and diluted to working concentrations of 10, 60, and 125 nM in a hybridization buffer. To demonstrate sequence capture specificity, chimeric *CCR5-CD4* ssDNA molecules containing bases 1–56 of the *CCR5* cDNA and bases 57–1377 of the *CD4* cDNA were used as a control. This particular region of the *CD4* cDNA was replaced because the capture and detection oligos were designed to bind to bases 1–20 and 36–56, respectively (Fig. S6†). While the fluorescence intensity from the MIM-MS containing the *CCR5-CD4* ssDNA control remained comparable to the background signal

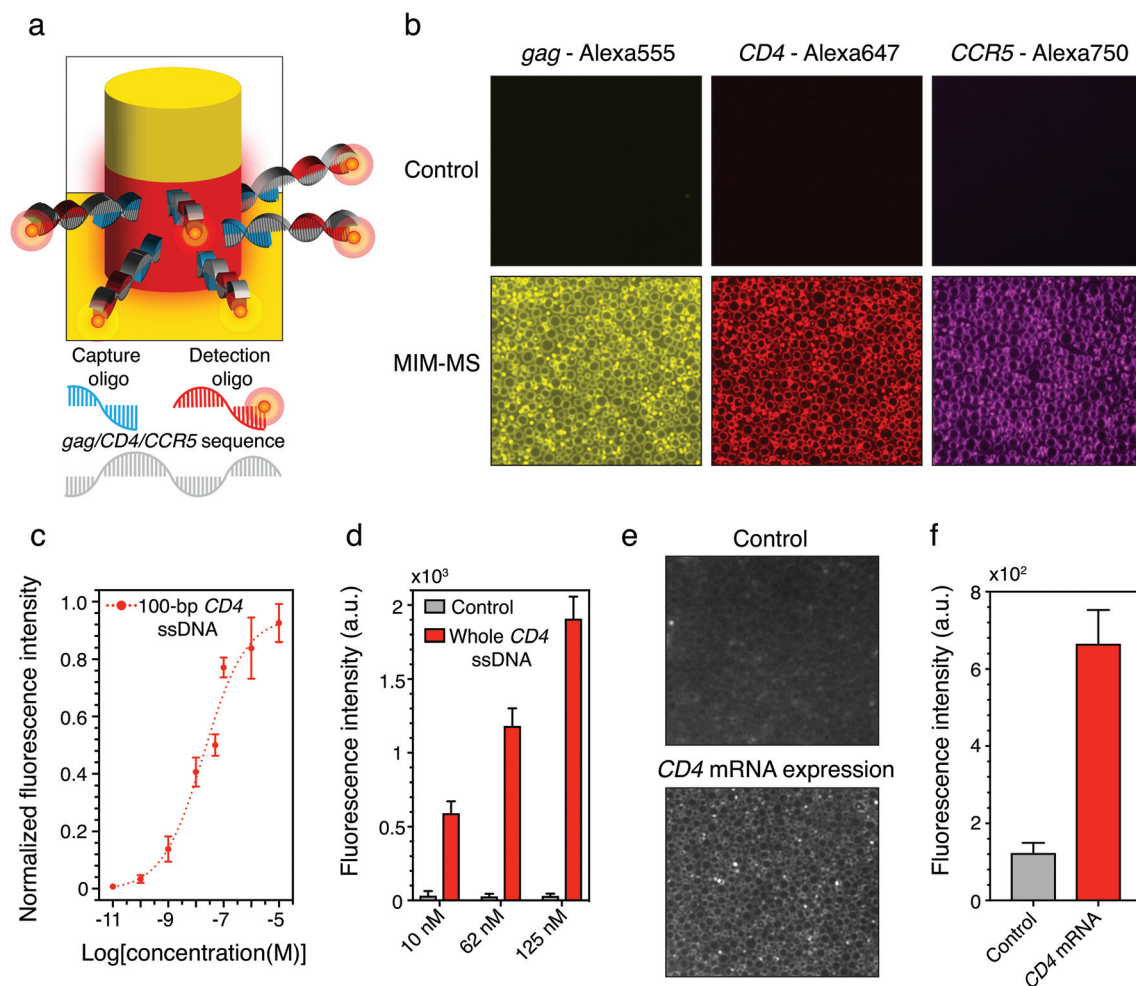


Fig. 5 (a) A schematic of the selective nucleic acid sequence detection assay. (b) Multiplexed detection of 100 bp *gag*, *CD4*, and *CCR5* sequences on MIM-MS with detection oligos conjugated with AF555, AF647, and AF790 compared to glass controls treated with the same conditions. (c) Normalized fluorescence intensity for the 100 bp *CD4* sequence captured at concentrations ranging from 10 pM–10 μ M. (d) Fluorescence intensity of a ssDNA analogue of the whole *CD4* gene captured and detected at concentrations of 10, 62, and 125 nM. In comparison, the negative control shows negligible change in fluorescence. (e) Fluorescent micrographs of the functionalized MIM-MS for the lysate of untransfected (control) and transfected cell cultures. (f) The sample overexpressing *CD4* mRNA displays a 5.4-fold higher average fluorescence intensity compared to the untransfected control.

for all three concentrations, the intensity for the full-length *CD4* ssDNA samples scaled by 1.9- and 2.6-fold for 60 and 125 nM compared to 10 nM (Fig. 5d). This indicates high specificity and scalability of the sandwich assay using the MIM-MS towards the detection of full-length nucleic acid molecules.

Finally, we tested if our MIM-MS sandwich assay protocol could specifically detect *CD4* mRNA molecules in total RNA samples derived from Expi293 cells. Total RNA was isolated from the lysate of Expi293 control cells and cells transiently-transfected to overexpress *CD4*. Initially, cell surface expression levels of the *CD4* protein were verified using flow cytometry (Fig. S9†). Although mRNA only represents a small fraction of total RNA,³⁹ and thousands of genes are expressed simultaneously in mammalian cells,⁴⁰ the MIM-MS sandwich assay was able to specifically detect full-length *CD4* mRNA molecules in the total RNA sample of the transfected cells. Compared to the control cells, the sample derived from the transfected cells

displayed a 5.4-fold increase in fluorescence (Fig. 5e and f). In a similar fashion, multiple genes of varying concentrations could be simultaneously isolated, detected, and quantified using this approach, making it a highly versatile platform for studying nucleic acids.

Conclusions

In summary, using a three-step biomimetic fabrication process, we have developed a highly scalable MIM-MS that consists of a dense array of closely-coupled Au nanodisks and nanoholes separated by 5 nm SiO_2 nanogaps. The higher-order quadrupolar gap mode of this configuration is highly radiant in the VIS-NIR regime, displays negligible absorptive losses, and suppresses quenching, making it highly suitable for supporting plasmon-enhanced fluorescence. The nanogaps can be

engineered to have sufficiently large usable surface areas which can be physically accessed and functionalized for bio-sensing applications. Utilizing these benefits, we conducted the multiplexed, substrate-enhanced biosensing of proteins (streptavidin–biotin complex) and nucleic acid sequences (*gag*, *CD4* and *CCR5*) of varying sizes (and therefore varying proximity to the plasmonic hotspot) and demonstrated the versatility of the MIM-MS in a practical application.

Conflicts of interest

There are no conflicts to declare.

Acknowledgements

The authors acknowledge the financial support provided by the SAMSUNG Global Research Outreach (GRO) program. The authors are also thankful for the support and resources provided by the Kavli Nanoscience Institute and the Beckman Institute Biological Imaging Facility at Caltech.

Notes and references

- 1 E. Purcell, *Phys. Rev.*, 1946, **69**, 681.
- 2 P. Goy, J. M. Raimond, M. Gross and S. Haroche, *Phys. Rev. Lett.*, 1983, **50**, 1903–1906.
- 3 D. Kleppner, *Phys. Rev. Lett.*, 1981, **47**, 233–236.
- 4 S. Kühn, U. Håkanson, L. Rogobete and V. Sandoghdar, *Phys. Rev. Lett.*, 2006, **97**, 017402.
- 5 P. Anger, P. Bharadwaj and L. Novotny, *Phys. Rev. Lett.*, 2006, **96**, 113002.
- 6 E. Dulkeith, A. C. Morteani, T. Niedereichholz, T. A. Klar, J. Feldmann, S. A. Levi, F. C. van Veggel, D. N. Reinhoudt, M. Möller and D. I. Gittins, *Phys. Rev. Lett.*, 2002, **89**, 203002.
- 7 R. Faggiani, J. Yang and P. Lalanne, *ACS Photonics*, 2015, **2**, 1739–1744.
- 8 J. Yang, R. Faggiani and P. Lalanne, *Nanoscale Horiz.*, 2016, **1**, 11–13.
- 9 N. Kongsuwan, A. Demetriadou, R. Chikkaraddy, F. Benz, V. A. Turek, U. F. Keyser, J. J. Baumberg and O. Hess, *ACS Photonics*, 2018, **5**, 186–191.
- 10 Y.-C. Chang, S.-M. Wang, H.-C. Chung, C.-B. Tseng and S.-H. Chang, *ACS Nano*, 2012, **6**, 3390–3396.
- 11 V. Flauraud, R. Regmi, P. M. Winkler, D. T. L. Alexander, H. Rigneault, N. F. van Hulst, M. F. García-Parajo, J. Wenger and J. Brugger, *Nano Lett.*, 2017, **17**, 1703–1710.
- 12 S. Tian, O. Neumann, M. J. McClain, X. Yang, L. Zhou, C. Zhang, P. Nordlander and N. J. Halas, *Nano Lett.*, 2017, **17**, 5071–5077.
- 13 A. Ruscito and M. C. DeRosa, *Front. Chem.*, 2016, **4**, 14.
- 14 F. Pfeiffer and G. Mayer, *Front. Chem.*, 2016, **4**, 25.
- 15 D. J. Javier, N. Nitin, M. Levy, A. Ellington and R. Richards-Kortum, *Bioconjugate Chem.*, 2008, **19**, 1309–1312.
- 16 Qubit RNA HS Assay Kit – Thermo Fisher Scientific, <https://www.thermofisher.com/order/catalog/product/Q32852>, (accessed October 16, 2018).
- 17 C. Huang, M. Moosmann, J. Jin, T. Heiler, S. Walheim and T. Schimmel, *Beilstein J. Nanotechnol.*, 2012, **3**, 620–628.
- 18 V. Narasimhan, R. H. Siddique, J. O. Lee, S. Kumar, B. Ndjamen, J. Du, N. Hong, D. Sretavan and H. Choo, *Nat. Nanotechnol.*, 2018, **13**, 512–519.
- 19 V. Saranathan, A. E. Seago, A. Sandy, S. Narayanan, S. G. J. Mochrie, E. R. Dufresne, H. Cao, C. O. Osuji and R. O. Prum, *Nano Lett.*, 2015, **15**, 3735–3742.
- 20 R. H. Siddique, J. Mertens, H. Hölscher and S. Vignolini, *Light: Sci. Appl.*, 2017, **6**, e17015.
- 21 E. Prodan, C. Radloff, N. J. Halas and P. Nordlander, *Science*, 2003, **302**, 419.
- 22 F. Tam, A. L. Chen, J. Kundu, H. Wang and N. J. Halas, *J. Chem. Phys.*, 2007, **127**, 204703.
- 23 R. Bardhan, N. K. Grady, J. R. Cole, A. Joshi and N. J. Halas, *ACS Nano*, 2009, **3**, 744–752.
- 24 P. K. Jain, K. S. Lee, I. H. El-Sayed and M. A. El-Sayed, *J. Phys. Chem. B*, 2006, **110**, 7238–7248.
- 25 C. M. Dundas, D. Demonte and S. Park, *Appl. Microbiol. Biotechnol.*, 2013, **97**, 9343–9353.
- 26 Z. Yang, S. Luo, H. Dai, J. Li, X. Jiao and X. Hu, *RSC Adv.*, 2013, **3**, 22868–22871.
- 27 A. K. Kenworthy, K. Hristova, D. Needham and T. J. McIntosh, *Biophys. J.*, 1995, **68**, 1921–1936.
- 28 W. A. Hendrickson, A. Pähler, J. L. Smith, Y. Satow, E. A. Merritt and R. P. Phizackerley, *Proc. Natl. Acad. Sci. U. S. A.*, 1989, **86**, 2190–2194.
- 29 N. M. Bell and A. M. L. Lever, *Trends Microbiol.*, 2013, **21**, 136–144.
- 30 M. J. Pace, E. H. Graf, L. M. Agosto, A. M. Mexas, F. Male, T. Brady, F. D. Bushman and U. O'Doherty, *PLoS Pathog.*, 2012, **8**, e1002818.
- 31 K. Wehrly and B. Chesebro, *Methods*, 1997, **12**, 288–293.
- 32 K. Murphy, C. Weaver and C. Weaver, *Janeway's Immunobiology*, Garland Science, 2016.
- 33 J.-C. Grivel, R. J. Shattock and L. B. Margolis, *J. Transl. Med.*, 2011, **9**, S6.
- 34 B. Lee, M. Sharron, L. J. Montaner, D. Weissman and R. W. Doms, *Proc. Natl. Acad. Sci. U. S. A.*, 1999, **96**, 5215–5220.
- 35 E. J. Platt, K. Wehrly, S. E. Kuhmann, B. Chesebro and D. Kabat, *J. Virol.*, 1998, **72**, 2855–2864.
- 36 J. Wang, K. Crawford, M. Yuan, H. Wang, P. R. Gorry and D. Gabuzda, *J. Infect. Dis.*, 2002, **185**, 885–897.
- 37 M. Pace and U. O'Doherty, *J. Infect. Dis.*, 2013, **207**, 1790–1792.
- 38 J. N. Zadeh, C. D. Steenberg, J. S. Bois, B. R. Wolfe, M. B. Pierce, A. R. Khan, R. M. Dirks and N. A. Pierce, *J. Comput. Chem.*, 2011, **32**, 170–173.
- 39 H. Lodish, A. Berk, S. L. Zipursky, P. Matsudaira, D. Baltimore and J. Darnell, *Molecular Cell Biology*, W. H. Freeman, 4th edn, 2000.
- 40 G. K. Marinov, B. A. Williams, K. McCue, G. P. Schroth, J. Gertz, R. M. Myers and B. J. Wold, *Genome Res.*, 2014, **24**, 496–510.